Space Weather®

RESEARCH ARTICLE
10.1029/2023SW003470

The Impact of Space Radiation on Brains of Future Martian and Lunar Explorers

Yuncong Li[1], Jingnan Guo[1,2,3], Salman Khaksarighiri[4], Mikhail Igorevich Dobynde[1], Jian Zhang[1], Bailiang Liu[1], and Robert F. Wimmer-Schweingruber[4]

[1]Deep Space Exploration Laboratory/School of Earth and Space Sciences, University of Science and Technology of China, Hefei, China, [2]CAS Center for Excellence in Comparative Planetology, USTC, Hefei, China, [3]Collaborative Innovation Center of Astronautical Science and Technology, Harbin, China, [4]Institute of Experimental and Applied Physics, University of Kiel, Kiel, Germany

Key Points:

- We model the dose in the head exposed to the Martian and lunar surface radiation environment
- We analyze the "brain" dose correlation between the Martian and lunar results
- We evaluate the space radiation risks for "brains" of future Martian and lunar explorers

Correspondence to:

J. Guo,
jnguo@ustc.edu.cn

Citation:

Li, Y., Guo, J., Khaksarighiri, S., Dobynde, M. I., Zhang, J., Liu, B., & Wimmer-Schweingruber, R. F. (2023). The impact of space radiation on brains of future Martian and lunar explorers. *Space Weather*, *21*, e2023SW003470. https://doi.org/10.1029/2023SW003470

Received 1 MAR 2023
Accepted 7 SEP 2023

Author Contributions:

Conceptualization: Jingnan Guo, Salman Khaksarighiri
Formal analysis: Yuncong Li
Investigation: Yuncong Li
Methodology: Jingnan Guo, Salman Khaksarighiri
Supervision: Jingnan Guo
Visualization: Yuncong Li
Writing – original draft: Yuncong Li, Jingnan Guo
Writing – review & editing: Yuncong Li, Jingnan Guo, Salman Khaksarighiri

© 2023 The Authors.
This is an open access article under the terms of the Creative Commons Attribution-NonCommercial License, which permits use, distribution and reproduction in any medium, provided the original work is properly cited and is not used for commercial purposes.

Abstract Astronauts will be facing many risks when they are away from Earth's environment, among which radiation is one of the most vital and troublesome issues. Space radiation exposure from energetic particles of Solar Energetic Particles (SEPs) and Galactic Cosmic Rays (GCRs) can adversely impact the Central Nervous System (CNS) by inducing acute (i.e., mission critical) and chronic (i.e., post-mission) effects, respectively. Recently, Brain Response Functions (BRFs) based on a realistic brain structure have been developed to model cosmic-ray induced dose in the brain (Khaksarighiri et al., 2020, https://doi.org/10.1016/j.lssr.2020.07.003). In this study, to quantify the radiation induced dose and evaluate the radiation risk to the CNS of the astronauts on the surface of Mars and Moon and in deep space, we use GCR/SEP spectral models together with Mars/Moon radiation transport codes to obtain the radiation field to which astronauts are exposed, and derive the absorbed dose in the brain with BRFs. Our calculations show that GCR induced absorbed dose per month in the brain does not reach the 30-day limit for CNS (500 mGy) as defined by NASA on either Martian or lunar surface. Based on the spectra and frequency of historical extreme SEP events recorded at Earth as ground-level enhancement events over past five solar cycles, our results suggest that the CNS of astronauts will be generally "safe" on the Martian surface, but those on the lunar surface or in deep space may face radiation risks in their CNS if not well shielded during such extreme events.

Plain Language Summary Among various concerns for the health of future astronauts exploring the Moon and Mars, space radiation-induced health risks cause one of the most urgent and vital problems for future missions. The astronauts will be exposed to the Galactic Cosmic Rays (GCRs) as background radiation and sporadic while potentially more hazardous Solar Energetic Particles (SEPs), which would leave energy and deposit dose in the human body of astronauts who may consequently suffer from a series of acute or post-mission health issues. Here we study the dose deposited in the brain when exposed in deep space or the lunar/Martian radiation environment induced by the above GCR and SEP radiation sources. In particular, the surface radiation environment of the Moon or Mars could be different from that in deep space due to particle interactions with the planetary atmosphere and/or regolith, which can be derived from the Monte-Carlo simulations. Finally, we calculate the resulting dose in a model with a realistic head structure. Our calculations suggest that during extreme SEP events, astronauts' CNS may face radiation risks in deep space or on the lunar surface if not well shielded, but it is generally "safe" for their brains on the Martian surface.

1. Introduction

Human space missions are one of the most important achievements and goals of space exploration activities. Various national space agencies or even private sectors are preparing to send astronauts back to the Moon within the next decade and eventually to Mars. With the goal of sending people back to the lunar surface and establishing a permanent human presence in cislunar space, the Artemis lunar exploration program will bring us a big step forward toward landing humans and sustainable crewed exploration on the Moon and further destinations (Smith et al., 2020). However, astronauts will face hazards including higher level of radiation due to the absence of protection of the Earth's magnetosphere, together with other health and performance risk sources such as microgravity, long periods of isolation and confinement, inadequate food and nutrition and so on. In particular, radiation risk is the most significant and unavoidable risk for astronauts' health, especially for their long-term stays at future bases on the Moon or Mars (Patel et al., 2020). Energetic particles of different types and energies in space or planetary surfaces are responsible for substantial biomedical or health risks (Chancellor et al., 2014;

Wu et al., 2013), including acute radiation syndrome, heart diseases (Boerma et al., 2015; Delp et al., 2016), Central Nervous System (CNS) issues, cataracts (Cucinotta et al., 2014) or long-term increased cancer risk (Huff Janice et al., 2016). In the human system risks evaluation approach, space radiation health effects of cancer, cardiovascular disease, and cognitive decrements form one of the "red-color" ranked risks, that have the highest priority based on both the likelihood of occurrence and the severity of their impact on human health, mission performance, and long-term life quality (Patel et al., 2020).

As the commander of the human body, the CNS, which is made up of the brain and spinal cord is of critical concern due to clinically significant acute risks and the late CNS risks such as Alzheimer's disease (Cucinotta et al., 2014). However, due to the scarcity of samples (only 24 astronauts in the Apollo mission went beyond the Earth's magnetosphere), as well as the impossibility of human experiments, the main difficulty remains in predicting and identifying biological and physical countermeasures under radiation exposure and in quantifying the acceptable level of radiation risks (e.g., Chancellor et al., 2014). It is therefore important to study space radiation and infer its potential impacts on future "space brains."

1.1. Radiation Environment in Deep Space

Beyond Earth's magnetosphere, the deep space radiation environment mainly consists of two parts: Galactic Cosmic Rays (GCR) as a continuous background and sporadic solar energetic particles (SEP) that are associated with solar eruptive events.

GCRs originate from outside the solar system, consisting of 87% protons, 12% helium ions and 1% heavier nuclei, including C, N, O, and Fe (Simpson, 1983). Particle energy ranges from around 1 MeV/n to TeV/n and above. GCR flux is modulated by solar activity, and is anti-correlated with the sunspot number. Although the flux of GCRs is relatively low compared to that of impulsive SEPs, protons and heavy nuclei especially with energies above GeV may be able to generate secondary particles from atomic and nuclear interactions with materials, which makes it rather difficult to shield against GCRs (Cucinotta et al., 2014). Considering also the long integration time of interplanetary missions such as to Mars, GCR radiation can be a threat to astronauts' health (e.g., Guo et al., 2021). A radiation risk assessment study estimates that 20 million out of 43 million hippocampus cell nuclei in the brain could be directly hit by one or more particles, with charge $Z > 15$ assuming the 1977 GCR spectrum (solar minimum condition) in a pressure vessel during a 3-year mission to Mars (Curtis et al., 1998).

SEPs, mainly protons and electrons, are accelerated by solar flares and/or CME-driven shocks during solar eruptions so that SEP events tend to occur more frequently during solar active periods. SEPs have energies from a few keV up to $\sim 10^3$ MeV and may have a very high fluence, which could induce a high level of dose within a short time duration and cause acute radiation syndromes especially under no-shielding circumstances (Hu et al., 2009).

Our work adopts models of GCRs and spectra of historical SEPs (see Section 2.1) to study the radiation dose level inside the brains of future Martian/lunar explorers.

1.2. Radiation Effects on Human Brains and the CNS System

During the early time of human space explorations, an unusual visual phenomenon was reported by Apollo astronauts, including streaks, flashes, and clouds "seen" by their eyes. It was revealed that fast neutrons and high-charge and energy (HZE) particles with Linear Energy Transfer (LET, dE/dx) greater than 10 keV μm^{-1} propagating through the retina and surrounding posterior portion (Budinger et al., 1972) can trigger Cerenkov light. This discovery raised further concerns about radiation damage to the CNS system. Clinical experience on the patients undergoing radiotherapy has found adverse changes in CNS behavioral disorders involving learning, memory, processing speed, attention, cognitive flexibility, executive function, and others that may cause anxiety and depression. Biomarker and mechanistic studies of CNS risks reveal clues of radiation damage pathogenesis, such as altered neurogenesis linked cognitive injury, neuroinflammation associated with Alzheimer's disease and Parkinson's disease, oxidative and radical damage, as well as signaling and neuro-transmitter changes induced neurocognitive impairment (Cucinotta et al., 2014). However, due to the absence of human data (with exposure to low or moderate deep space dose rate) in this research field, the threshold radiation criteria for clinically significant CNS effects remains to be understood (Chancellor et al., 2014). The impact to neurocognitive and behavioral health as well as performance resulting from the interaction of space radiation with other mission hazards is also critical to be studied (Patel et al., 2020).

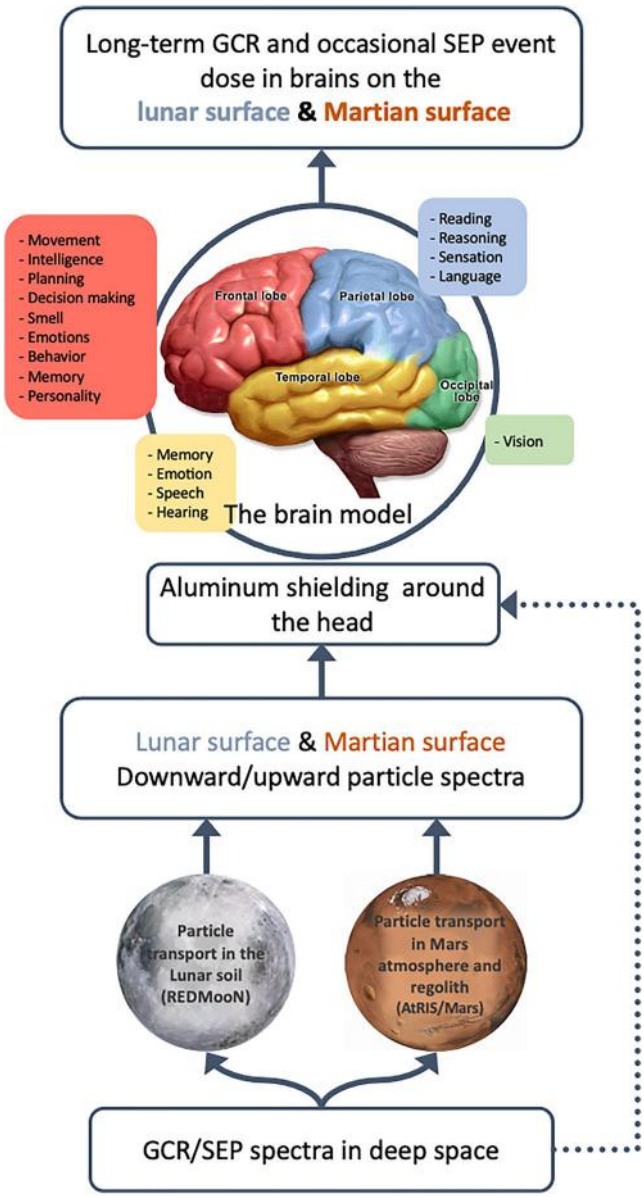

Figure 1. Methods of calculating dose induced by energetic particles (either Galactic Cosmic Rays or Solar Energetic Particles) reaching "brains" on the surface of the Moon and Mars. In addition, energetic particles can directly impact the brain in deep space (the dotted line). The particle interaction with the lunar and Martian environment is calculated via the REDMoon model and AtRIS/Mars model, respectively. After arriving at the Moon, Mars or a space vessel in deep space, these particles can further reach and interact with human brains (which may be surrounded by some Aluminum shielding) and deposit dose therein. This is further calculated using the Brain Response Functions.

Extrapolations of radiation studies from rats and mice to humans suggest that cognitive detriments are caused by the brain area irradiation such as in the striatum, hippocampus (relative to learning and memory), and the pre-frontal cortex (Acharya et al., 2019). High levels of cosmic radiation exposure in animal models and experiments may cause impairments in cellular signaling in the hippocampus and damage in short-term memory (Parihar et al., 2016). Low dose rates of HZE-particles exposure accumulated over a long mission period may reduce the capacity of performing complex executive functions, as result of the loss of functionality in the pre-frontal cortex of mice (Lonart et al., 2012). Moreover, neuroinflammation, reduction in dendritic complexity and oxidative and radical damage are also seen as CNS effects under radiation, which lead to decrements in recognition memory, compromised cognitive performance and higher risk of neurodegenerative diseases of mice (Jandial et al., 2018; Parihar et al., 2016). The field of neuroepigenetics gives evidence that persistent changes in DNA methylation may significantly impact learning and memory and that increased levels of 5-methylcytosine (5mC) and 5-hydroxymethylcytosine (5hmC) in the hippocampus caused by cosmic radiation exposure is correlated with persistent impairments in hippocampal and cortical memory (Jandial et al., 2018). It is noteworthy that although animal models and experiments play a vital role in studies of space radiation risks in CNS, there may be limitations and uncertainties in extrapolating these findings to human organs, due to the intrinsic differences between various species and possible differences in response to radiation in space between human and experimental animals.

Driven by the urgency of understanding the impact of radiation on future astronauts exploring Mars and the Moon, we adopt the state-of-the-art GEometry ANd Tracking (GEANT4)-based particle transport models to calculate the Martian and lunar surface radiation environments. For the first time, the expected absorbed dose inside "an astronaut's brain" which is adapted from a realistic brain geometry is derived considering energetic particles (including protons, neutrons, and some HZE particles which have a significant contribution to dose) on the surface of the Moon/Mars or in deep space. Besides, different thicknesses of aluminum shielding around the human head are also considered in each scenario. The article is organized as follows: Section 2 introduces and describes the methods, model setup, and input parameters for the study; Section 3 shows and discusses the results and Section 4 summarizes the main results and shows a further discussion.

2. Method

The method used in this paper includes four parts: primary GCR and SEP spectra, AtRIS/Mars model, the REDMoon model, and the Brain Response Functions (BRFs). GCRs and SEPs are space radiation sources considered in this work as described in Section 2.1. They reach the vicinity of Mars (or Moon) and interact with the Martian (or lunar) radiation environment. This process can be modeled in detail using particle transport models (Section 2.2) and hereby we use two recently developed and validated models: AtRIS/Mars model (Guo et al., 2019; Section 2.3) and the REDMoon model (Dobynde & Guo, 2021b; Section 2.4). After reaching the astronauts on the surface of Mars or Moon or in deep space, these particles can further interact with the shielding and the brains inside to cause potential radiation hazards. This process is further modeled using the BRFs (Khaksarighiri et al., 2020; Section 2.5). The overall procedure combining three models is shown in Figure 1.

2.1. The Primary GCR and SEP Radiation

GCR spectra used in this study are derived from the 2014 Badwhar O'Neil 2014 model (BON14, O'Neill et al., 2015). It numerically solves the Fokker–Planck equation of GCR particles with diffusion, convection, and adiabatic deceleration as they traverse from the outer edge of the heliosphere into the vicinity of Earth. The radial gradient of GCR flux is only in the order of 1%–2% between 1 and 1.5 AU according to multiple spacecraft observations (Honig et al., 2019; Roussos et al., 2020), and therefore we assume that the GCR flux is the same at the vicinity of the Moon and Mars as predicted by the BON14 model for Earth. The BON14 model considers the solar activity by a solar modulation parameter (Φ) which represents the modulation strength of the heliospheric magnetic fields against the inward propagating GCRs. Its typical values range approximately from 350 MV for solar minimum to 1,200 MV for solar maximum. In this paper, we obtain the monthly GCR spectra considering monthly average Φ values associated with the BON14 model.

During the most energetic SEP events, protons of energies up to GeVs and above can contribute to the Earth's surface particle fluxes and be detected through ground-based neutron monitors, during so-called ground-level enhancement (GLE) events (e.g., Miroshnichenko et al., 2013). As for evaluation of SEP induced dose, we use solar proton spectra of 65 GLE events from 1942 to 2012 with the time-integral spectra of each event fitted with a double power law function based on four parameters (i.e., Band functions) (see Table 2 of Raukunen et al., 2018). These SEP fluxes are derived based on observations of detectors in space and ground-based neutron monitors at various geomagnetic cutoff rigidities. We also assume that these SEP events have arrived at Mars with the similar fluence as that measured near the Earth. This assumption is certainly not accurate, in particular for individual event, considering the transport feature of SEPs and the varying locations of Mars and Earth. However, here we consider the input radiation reaching the Moon and Mars to be the same for better evaluating and comparing the influence of the planetary environment on the radiation.

2.2. Particle Transportation Codes

Reproducing particle spectra on the planetary surfaces with the transport codes is an effective way to replicate the lunar and Martian radiation environment. GEANT4 (Agostinelli et al., 2003; Allison et al., 2006, 2016), FLUctuating KAscade (FLUKA) (Battistoni et al., 2015), Monte Carlo N-Particle (MCNP6) (Werner et al., 2017), and Particle and Heavy Ion Transport code System (PHITS) (Sato et al., 2013) are all general-purpose Monte Carlo codes used for simulating the movement and interaction of numerous particles over broad ranges of energies through materials, and have all been used for simulating space particle propagation through matter. All of these MC codes include various models to describe different interactions regarding different species of particle and energy ranges. A summary of physics models adapted by these codes is shown in Appendix A in Zaman et al. (2022). In particular, GEANT4 provides a large number of so-called physics lists describing the nuclear and atomic interactions of particles with matter, and the selection of the lists is based on the recommendations given by the GEANT4 community for specific applications.

NASA's analytic code HZETRN/OLTARIS (Slaba et al., 2016; Wilson et al., 2016) is another powerful tool used to simulate energetic particle transport and radiation effects on the human body. Unlike the Monte-Carlo codes, which employ a probabilistic approach to simulate particle interactions, HZETRN/OLTARIS uses a deterministic approach. It calculates particle transportation through materials by providing numerical solutions to the time-independent, linear Boltzmann equation. While this approach can be highly computationally efficient for certain types of simulations, it has its limitations, particularly when dealing with complex physical systems and geometries.

Matthiä et al. (2016) shows a comprehensive comparison between experimental data from the Radiation Assessment Detector (RAD, Hassler et al., 2014) at the surface of Mars and model calculations from 2D HZETRN/OLTARIS, PHITS, OLTARIS2013, and GENAT4 with different physics lists. Overall, particle spectra calculated by GEANT4 with suitable selection of physical models reveal best agreement with the measurement among all of the Monte-Carlo codes. The proton, ^{4}He, and heavier nuclei with nuclei less than 14 results of PHITS is also compatible with that of GEANT4 and reproduces the measured deuteron flux nicely. Similarly, Zaman et al. (2022) compared the lunar surface radiation environment simulation results from FLUKA, GEANT4, MCNP, PHITS, etc. The results of this work show overall good agreement between the codes. However, there are disagreements existing in some areas, for example, GEANT4 shows a relative overestimation of low-energy electrons, which are probably created by Compton scattering.

2.3. Modeling Mars Surface Radiation With AtRIS/Mars

In order to derive the particle spectra on the surface of Mars from those in deep space, we use a GEANT4-based planetary particle transport simulation tool called Atmospheric Radiation Interaction Simulator (AtRIS, Banjac et al., 2018; Guo et al., 2019). AtRIS has been applied to Mars and validated to be consistent with the particle flux measurements by RAD within the Gale crater on Mars and the preferred physics list of GEANT4 has been found to be FTFP_INCLXX_HP (Guo et al., 2019). In the model, Mars is a geometric sphere with a radius of 3,390 km, consisting of a 100-m-thick crust sheet composed of 50% Si, 40% O, and 10% Fe with a density of 1.79 g/cm^2. Above the spherical surface is a 100 km-thick atmosphere with an density and composition profile obtained by (MCD, Forget et al., 1999, http://www-mars.lmd.jussieu.fr) with more than 95% of the molecules are CO_2, as well as other elements including C, O, N, Ar, and H. The results-relevant surface pressure in Sections 3.1, 3.2, and 3.4 is fixed in 827 Pa, which is the value averaged over different seasons in the Gale crater as measured by the Curiosity rover. The influence of different pressures (ranging from 82 to 1,200 Pa) on the surface radiation has been investigated by Zhang et al. (2022) which shows that the quiet-time GCR radiation on Mars surface is not very sensitive to the surface pressure. However, we will show that GLE-induced surface dose can be dependent on the surface pressure conditions as demonstrated in Section 3.5.

Atmospheric response matrices (ARMs) make AtRIS a convenient tool to simulate the Martian radiation environment (Banjac et al., 2018). ARMs are obtained through the simulation of primary particles through the atmospheric model for different primary-secondary cases (e.g., protons producing neutrons) and directions (upwards and downwards). AtRIS calculates the average ionized effect of a particle with a specific energy penetrating each layer of the atmosphere, and lists resulting different secondary particles with different energy-histograms. Directionality of the secondary particles, such as upward or downward, can also be scored by using multiple histograms. Consequently, each column of an ARM represents a histogram of secondary particles of a certain direction which are created by primary particles with one certain energy. Secondary particle spectrum can be obtained simply by multiplying the incoming GCR/SEP spectrum with the matrix, rather than running new simulations each time considering a new cosmic ray spectrum (Guo et al., 2019). In this study, we utilize surface protons, neutrons, alphas, and several HZE (e.g., C, N, Fe) spectra in upward and downward directions after convoluting GCR and GLE spectra with the ARMs.

2.4. Modeling Lunar Surface Radiation With the REDMoon

The Moon lacks a global magnetic field and has no atmosphere, thus particles would directly enter the soil and generate an albedo component, making the lunar radiation field different from that in deep space the Radiation Environment and Dose at the Moon model (REDMoon, Dobynde & Guo, 2021b) is a GEANT4 code and response function approach-based model used to simulate the lunar surface and subsurface radiation environment. It is similar to AtRIS/Mars, but set up with the lunar regolith environment following the McKinney et al. (2006) with mainly Si, O, and other elements such as Mg and Al, and no atmospheric influence on the energetic particles is considered. Besides, the REDMoon model also takes into account the incoming zenith direction divergence of the particles.

In the procedure of calculating the secondary particle flux, the REDMoon response function requires three input parameters, which are primary particle type (ions with $Z = 1{:}28$), particle energy, and zenith angle of incidence on the lunar surface. As a result of the convolution of the primary particle spectrum with the response function, we obtain secondary particle flux of a certain particle type, as a function of energy, zenith direction, and soil depth. The surface albedo spectra predicted by the REDMoon agree well with previous experimental and numerical studies (Dobynde & Guo, 2021b). In this paper, we utilize the lunar surface upward albedo spectra (first output layer) of protons and neutrons together with the primary downward GCR and SEP spectra as the lunar surface radiation environment.

2.5. Modeling Radiation in a Brain Using Brain Response Functions

To calculate the BRFs, a voxelized geometry of a real human head containing the whole brain structure has been reconstructed using 134 slices of CT images (Khaksarighiri et al., 2020). Based on this actual human head structure, GEANT4 simulations have been performed to simulate the dose distribution within the human head. Besides, additional aluminum shielding is also considered: different thickness of aluminum shell is added

between the head and particle source in each shielding scenario. Similar to the ARM approach, Khaksarighiri et al. (2020, 2021) simulated and calculated the BRFs representing the dose of a given primary particle depositing inside the human head and also different parts of the brain. In other words, a BRF is a probabilistic description of all possible interactions of particles with the matter as they pass through the head structures and gives the energy deposited in different parts (i.e., lobes) of the brain from a primary particle with specific energy and type. Note that the secondaries generated in particle interactions with the brain structure additionally contribute to absorbed dose and are also included in the BRFs. Plus, in the shielding scenario, the contribution to the brain dose by secondaries generated in the Al-shield (due to the source particles interacting with the shield) is counted into the corresponding BRFs as well.

We utilize the BRFs for incoming protons, neutrons, helium ions, and some heavier ions such as carbon, nitrogen, and iron nuclei for different lobes (including the frontal lobe, occipital lobe, and others) of the brain. These primary HZE particles are chosen due to their large abundance and biological relevance in deep space radiation environment. Specifically, the recent ground-based experiments (Cucinotta et al., 2014; Rivera et al., 2013) show that irons contribute significantly to CNS risks, therefore the iron-induced doses are simulated as well. These functions can be convoluted with energetic cosmic-ray particle spectrum (e.g., on the surface of the Moon or Mars) to obtain the absorbed dose rate distribution inside human brains thereby. Mathematically, the procedure can be summarized as given below,

$$D_{ij} = \sum_k B_{ij}(E_k) f_i(E_k) W_i(E_k) = \sum_k B_{ij}(E_k) F_i(E_k), \quad (1)$$

$$D_j = \sum_i D_{ij}, \quad (2)$$

where D_{ij} is the dose induced by particle type i in the brain lobe j. B_{ij} is the BRF in the lobe j of particle i in the unit of μGy/(particles/cm^2/sr). f_i is the spectrum (e.g., with the unit of particles/cm^2/sr/MeV) of a given GCR/SEP spectrum of particle i. W_i is the bin width of B_i in the unit of MeV, which is multiplied with f_i to obtain F_i with the unit of particles/cm^2/sr. The deposited dose induced by particle i, D_{ij}, is then obtained after summing over k energy bins of the BRF. Finally, the total dose in the lobe j, D_j, can be acquired by summing up doses induced by different particles types of the GCR/SEP event.

It is worth to mention that the BRF results in Sections 3.2, 3.3 and Figure 6a in Section 3.4 actually refer to the dose in the entire head including the skull, we take the results as the "brain" dose which would be slightly larger than the actual dose in the brain due to the higher density and outer location of the skull. This difference will be shown and discussed later in Section 3.4 and Figure 6b. This means that our risk estimation is a conservative assessment.

3. Results

3.1. Martian and Lunar Surface Radiation Environment

As shown in the first two steps of Figure 1, using the AtRIS/Mars (Section 2.3) and the REDMoon (Section 2.4) models, we obtain a series of particle spectra on the Martian and lunar surfaces induced by both background GCRs and past GLE events and the results are shown in this subsection. In particular, we will focus on discussing the spectra of three types of secondary particles, protons, alpha particles, and neutrons, which make the major contribution to the absorbed dose.

3.1.1. Background GCR Radiation Field

Figure 2 shows GCR-induced particle flux on the surface of Mars and Moon in either the downward or upward direction with orange for Martian results and purple for lunar results. Not all simulated particles are plotted while the three most important ones, surface protons, alphas, and neutrons, are shown. The transparent color bands represent spectral results under a virtual solar cycle period, during which the minimum and maximum solar modulation parameters Φ are 427–1,377 MV, respectively, based on historical records from solar cycle 19 to 23. The results under a typical value of Φ = 550 MV as input spectra (see Section 2.1) are shown in the

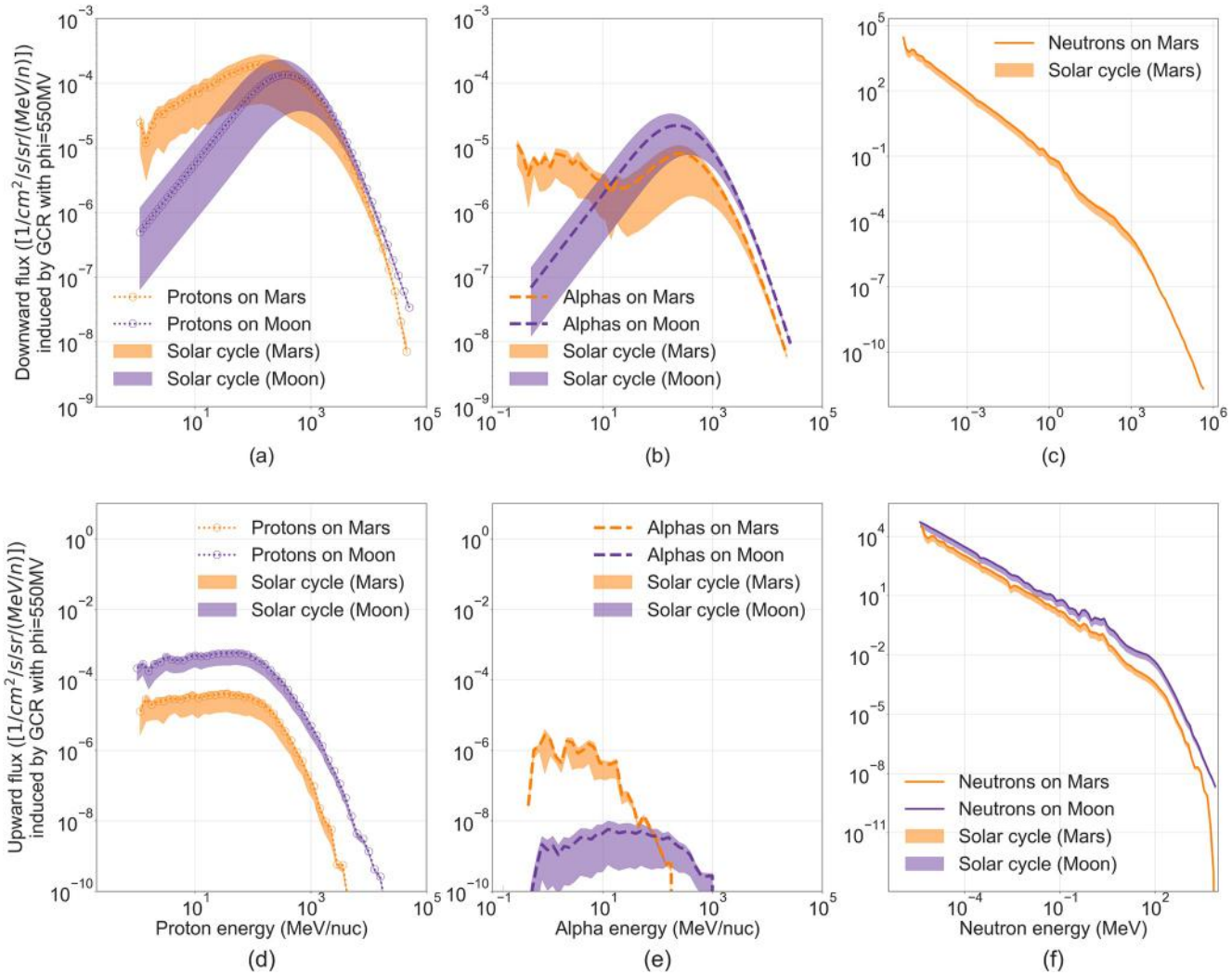

Figure 2. Downward (top panels) and upward (lower panels) proton, alpha, and neutron spectra induced by Galactic Cosmic Rays on the surface of Mars (with a surface pressure of 827 Pa, orange lines/bands) and Moon (purple, lines/bands). Highlighted color bands cover outcomes covering the minimum and maximum modulation conditions, and the results under solar modulation parameter of 550 MV are lines located within the band. "Solar cycle" in labels means one virtual solar cycle with the minimum and maximum solar modulation parameters selected through solar cycle 19 to 23.

deeper-colored lines. This Φ value is chosen following Guo et al. (2019) where the authors validated the Mars/AtRIS model against the Mars surface measurement during a period with an average Φ of 550 MV.

Protons, the most abundant particle component of GCRs, constitute the most significant part of both the Martian and lunar radiation environment as also shown in Figure 2. In the downward direction, Martian surface proton differential flux peaks at ~200 MeV (panel a), which is slightly higher than the atmospheric cutoff energy of about 160 MeV for the considered atmospheric pressure. The cutoff energy represents the energy for a proton needed to penetrate the Martian atmosphere and arrive at the surface (Guo et al., 2019). In the high energy range (above a few GeVs), proton flux on the Martian surface is slightly lower than that on the Moon suggesting that the Martian atmosphere can slow down or interact with these energetic particles. For protons with lower energies <~300 MeV, however, the Martian surface (according to results of AtRIS) shows a higher flux compared to the original GCR proton spectrum (also the downward proton spectrum on the lunar surface). This is because the more energetic protons may lose energy when propagating through the Martian atmosphere and reach the ground with lower energies at ~100 MeV, and also other heavier particles (i.e., alphas) may fragment into less energetic protons.

Meanwhile, an upward proton component is produced in the planetary regolith via the interaction of high-energy particles reaching the planetary surfaces to generate secondaries which are then scattered upward. The shapes of

the albedo spectra on Mars and Moon are very similar as shown in panel (d). In the low-energy range, say, below the peaks at about 70 MeV, albedo protons on the Moon have a much higher flux than the downward flux, mainly contributed by the abundant generation by higher-energy downward protons in the soil. Overall, upward proton flux on the lunar surface exceeds that on Mars by about one order of magnitude. Comparing the downward particle spectra on the Moon and Mars which are responsible for generating the upward albedo components (panels a and b), we suggest that these upward protons are mainly generated by protons above a few hundreds of MeV or high-energy alpha particles as their fluxes are higher on the Moon.

For alphas, as shown in panel (b), flux on the Martian surface exceeds that on the lunar surface below about 10 MeV due to the fragmentation and spallation reactions of protons and HZE of higher energies with the nucleus in the atmosphere. But the Lunar-surface downward alpha flux is generally higher than the Martian one at higher energies mainly due to the fragmentation process of alphas through the Martian atmosphere. Panel (e) compares the upward alphas on the surfaces of Mars and Moon which shows that the flux on Mars is higher than that on the Moon by more than one order of magnitude below about 10 MeV. And we notice similar features of the downward and upward alpha flux level at the <∼10 MeV range which suggests these particles may have the same physical origin, for example, they are generated via the spallation processes in the atmosphere with some particles scattered upward. In comparison, the lunar upward alpha spectrum extends to a larger energy range and this is probably because more higher energy particles reach the lunar surface than the Martian surface (e.g., shown in panel a and b) to generate albedo alphas with higher energies in the lunar regolith. It is worth noting that the current AtRIS/Mars model adopted the physics list FTFP_INCLXX_HP has a higher efficiency in generating secondary particles via spallation process (Guo et al., 2019) than the physics list FTFP_BERT_HP adopted by the current run of REDMoon. Nevertheless, for the calculation of dose which is the main focus of this study, these alpha particles make a very small contribution.

Finally, as shown in panel (f), albedo neutrons on the Moon and Mars are very similar in spectral shapes with the Martian upward neutron flux slightly lower than the lunar flux suggesting that they are primarily induced by downward high-energy protons (above ∼1 GeV) which have similar fluxes on the Moon and Mars. On Mars, as seen in panel (c), there is an extra downward neutron component which is generated in the atmosphere of Mars. It is important to note that low-energy neutrons (below about 10 MeV) from direct interactions, spallation collisions, or neutron evaporation can contribute significantly to the human-body effective dose which is a critical concern for human Mars/Moon missions (Adams et al., 2007; Köhler et al., 2014; Röstel et al., 2020).

3.1.2. Extreme SEP-Induced Radiation Field

Figure 3 shows proton and neutron flux on the Martian and lunar surfaces induced by 65 GLE events from 1956 to 2012 (see Section 2.1 and Raukunen et al., 2018). Since the Moon is in the vicinity of Earth and it lacks an atmosphere to interact with the space radiation, the originally-derived GLE spectra are considered as the downward proton spectra on the lunar surface as shown in Figure 3a. After interacting with the thin atmosphere of Mars, the proton flux has a significant decrease below ∼200 MeV which is consistent with the atmospheric cutoff energy at about 160 MeV. In the higher energy range (>∼200 MeV region), the proton flux on the Martian surface starts to approach that in deep space but is always slightly lower, suggesting that higher energy particles are less probable to interact with the atmosphere to lose their energy.

In the upward direction, as shown in Figure 3c, proton flux on the Martian surface is lower than that on the lunar surface by at least one order of magnitude. Both spectral shapes are relatively flat below about 100 MeV with a smooth transition toward a power-law at higher energies and the slope is slightly steeper for Mars than for the Moon.

Concerning the results of GLEs, both Martian and lunar modeled results show similarities in GLE-induced albedo neutron spectra (Figure 3d) while there is an additional downward neutron component on Mars surface as a result of the atmospheric interactions with the incoming radiation (Figure 3b). Since the neutron spectra have rather consistent shapes between different cases, we fit the neutron flux with a power-law function $F_n = c_1 \cdot E^{c_2}$ in the relatively low-energy range (where a power-law function can be applied) for both GCR- and GLE-induced neutron spectra. We use the GCR-induced neutron spectra in Figure 2 and neutron spectra induced by GLE event on 28 May 1990, whose flux is in a mid-range among different event spectra shown in Figure 3. The fitted parameters of the power-law are shown in Table 1 for different cases. The upper energy for most cases is about 10 MeV, except for the Martian downward GLE-induced spectra, which is about 100 MeV. As shown in the

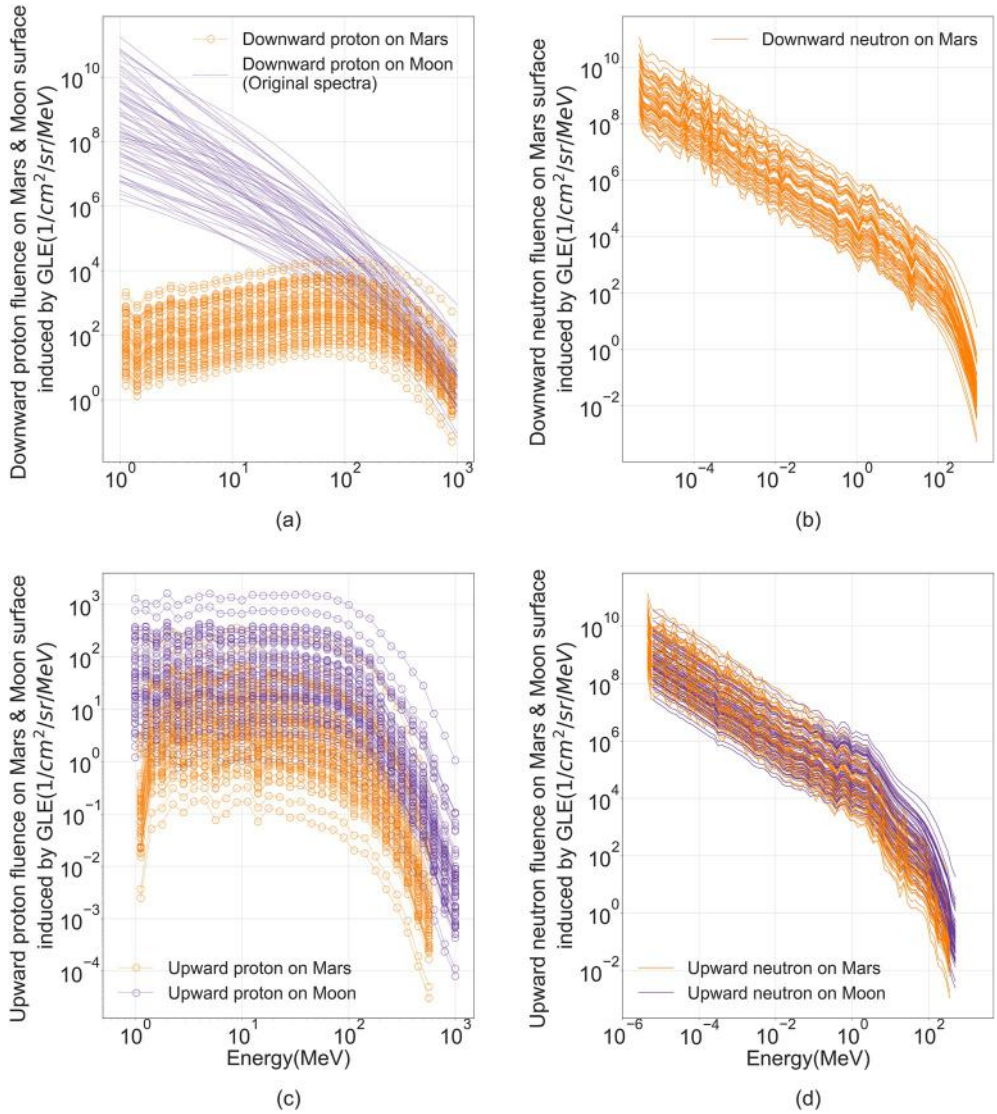

Figure 3. Proton and neutron spectra in downward (panels a and b) and upward (panels c and d) directions induced by 65 selected ground-level enhancement events. Orange lines/circles are for Martian surface spectra with a surface pressure of 827 Pa and purple lines are for the lunar surface results.

Table 1
Parameters, Energy Range and Standard Error of Two Parameters of the Power-Law Fit in Selected Neutron Spectra Which Are Galactic Cosmic Rays (GCR)- or Ground-Level Enhancement (GLE) (28 May 1990)-Induced Neutron Flux on the Martian and Lunar Surface

	Energy range (MeV)	c_1	c_2
Martian downward GCR	10^{-5}–10^{1}	$e^{-2.46\pm0.058}$	-1.00 ± 0.009
Martian upward GCR	10^{-5}–10^{1}	$e^{-1.95\pm0.052}$	-0.97 ± 0.008
lunar upward GCR	10^{-5}–10^{1}	$e^{-11.06\pm0.041}$	-0.89 ± 0.005
Martian downward GLE	10^{-5}–10^{2}	$e^{-11.44\pm0.045}$	-0.91 ± 0.007
Martian upward GLE	10^{-5}–10^{1}	$e^{-11.71\pm0.052}$	-0.90 ± 0.008
lunar upward GLE	10^{-6}–10^{1}	$e^{-11.65\pm0.063}$	-0.77 ± 0.009

table, the Martian downward GCR-induced spectra have the steepest (softest) power law with $c_2 = -1.0$, while the lunar GLE-induced upward spectrum has the most flat (hardest) power law with $c_2 = -0.77$. For GLE events, the fitted c_1 are certainly different for different events with different fluence, but the power-law index c_2 should be very similar observing the spectral shape distribution in Figures 3b and 3d.

In addition to the spectra presented here in Section 3.1 of protons, neutrons, and alpha particles, GCR HZE ion spectra have also been obtained from our models either in the lunar downward GCR components or as secondary composition on the Martian surface. Examples of the HZE secondary spectra on Mars can be found in a recent study by Zhang et al. (2022) while those on the Moon have been shown in Dobynde and Guo (2021b). Following the procedure introduced in the BRF section, we further consider these lunar/Martian surface particles to be transported in the head and brain structure

(Figure 1) with/without the Al shielding around the head and the final deposited dose (or dose rate) is calculated for "future brains" exposed on the surface of the Moon or Mars, as shown in the next subsection.

3.2. Radiation Exposure of Brains on the Martian Surface

The "brain dose" on the Martian surface is the result of convolution of surface particle spectra (both those shown in Section 3.1 and secondary HZEs on Mars) with the corresponding BRFs for each particle type hitting the "head." Note that the HZE-induced dose (of C, N, and Fe) is also taken into consideration despite that HZE flux is much lower compared with the proton flux due to absorption of the Martian atmosphere. Downward and upward fluxes are considered separately in the above procedure with each occupying half of the full 4π-solid angle and the total dose is the sum of the two directions and of different particle types.

The dose (or dose rate) induced by each GLE event (or GCRs) from 1952 to 2012 over more than five solar cycles (from the end of Cycle 18 to the first half of Cycle 24) is shown in Figure 4, where the monthly sunspot numbers are also plotted to demonstrate the solar activity evolution over the cycles. The unit of the BRF is μGy/particle fluence following Equation 1, and the input GLE spectra are also integrated over the duration of each event. So the GLE results in Figures 4–7 are the doses induced through the entire period of each event. The input GCR and GLE fluxes arriving at Mars or the Moon are assumed to be isotropic and we consider neither Mars nor the Moon has an effective magnetosphere to modulate the energetic flux at different locations of the planet. Nevertheless, variations in the results of GLE doses due to changes of the Martian pressure are discussed in Section 3.5. For results before that section, the surface pressure is fixed as 827 Pa. Note that no extra shielding around the astronauts are considered in the results plotted here and the shielding effect will be considered in Section 3.5.

International Commission on Radiological Protection (ICRP) divided radiation effects into stochastic effects and deterministic effects. For stochastic effects, limits are set to keep the risk of exposure-induced death less than 3% from fatal cancer for career exposure (Cucinotta, 2010), and the risk estimation is based on ground-based occupational experience. Deterministic effects include clinical radiation effects experienced after a threshold dose is exceeded and continue to change in severity with dose. In this study, we adopt the NASA dose limit for short-term or career non-cancer effects in CNS as criteria to evaluate the risk of space radiation impact on a brain, that is 500 mGy for the 30-day limit (Cucinotta, 2010). In Figure 4, curves and bars in blue (instead of red) mean that monthly accumulated GCR- and GLE-induced dose is within this safe range for CNS.

The dose rate induced by GCRs in a human head, varies with the solar cycle and ranges from 0.032 (in 1959) to 0.120 (in 2010) mGy/day. Referring to a possible NASA design reference mission (Drake et al., 2010), GCR-induced dose in solar minimum during a 500-day surface stay is in the range of 16 and 60 mGy, which is still within the 30-day limit in the CNS system. The evolution of the Martian surface dose in the head is anti-correlated with the sunspot number, with a slight delay in its temporal variation. This follows the expectation since the transport of GCRs in the interplanetary space is modulated by the heliospheric magnetic field which follows the solar activity cycle featured by the sunspot number (e.g., Potgieter, 2013). When solar activity and solar modulation become weaker (or stronger), there is an increase (or decrease) of GCR fluxes, particularly in the below-GeV part of the spectra (see the purple downward fluxes in Figures 2a and 2b). The delay of the variation is due to the fact that the observed GCR variation is a combined result of the varying interplanetary magnetic field and the inward propagating charged particles while both had a delay after the sunspot variation (e.g., Cliver & Ling, 2001; Thomas et al., 2014; Wang et al., 2022), although the exact process quantifying this delay is still under debate.

On the other hand, the frequency and intensity of GLE events only roughly follow the evolution of solar cycle activity, which is depicted by sunspot numbers. Figure 4 shows that the GLE dose level distribution is highly unpredictable across different solar cycles. Cycle 20 and cycle 21 showed relatively low dose for each GLE event, while events with conspicuously high dose occurred during cycles 19, 22, and 23. Among all of the 58 days with event occurrence, the event doses range from 0.05 to 33.50 mGy/event, while most of the events (about 60%) induced dose below 1 mGy. None of past GLE events induced dose higher than 500 mGy on the surface of Mars.

3.3. Radiation Exposure of Brains on the Lunar Surface

Following a similar procedure of Martian surface radiation dose calculations in Section 3.2, we also calculate and plot the lunar-surface dose (rate) profile in Figure 5. On the surface of the Moon, half of the radiation source is the

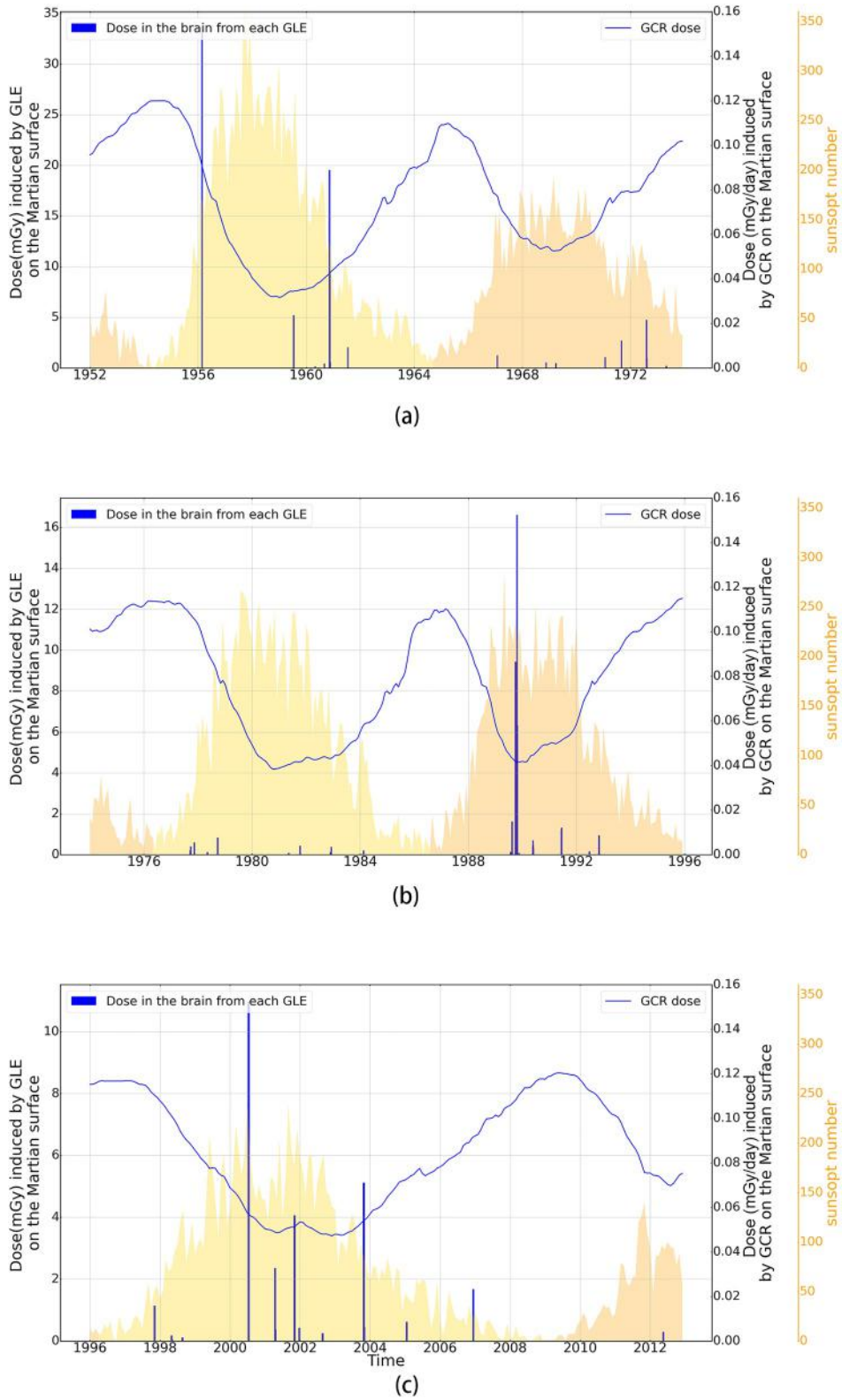

Figure 4. Long-term variations of dose (or dose rate) induced by Galactic Cosmic Rays (blue lines, right *y*-axes) and by each ground-level enhancement event (blue bars, left *y*-axes) over more than 5 solar cycles on the Martian surface with a surface pressure of 827 Pa. Sunspot numbers are plotted as yellow (odd cycle) and orange (even cycle) backgrounds.

original deep space radiation (downward component) while the other half (upward component) is the lunar albedo radiation (e.g., Dobynde & Guo, 2021b). Our calculations show that the GCR dose rate ranges from 0.039 to 0.184 mGy/day and the monthly-integrated GCR dose in the brain on the Moon stays under the 500 mGy 30-day limit. However, due to the lack of atmospheric shielding, the GLE-induced dose can reach up to 8,214.02 mGy/event for the 1972 August 4 event, and there are 13 events above the CNS 30-day limit of 500 mGy.

Again, we note that event-dose level shows great variance at the same phase of solar cycles among each GLE event, which reflects the irregularity of SEP events and the unpredictability of their scales. During periods with frequent event occurrence, the 30-day limit can also be reached even if single events are below this limit, such as during October 1989. However, these dose results are calculated with no shielding around the head which seems to be an unrealistic scenario, that is, the "brain" is only protected by the skull of the head while no space helmet/habitat shielding is considered. Results with shielding considerations will be discussed in Section 3.5.

3.4. The Correlation Between the Martian and Lunar Results

Figure 6a shows the correlation between the brain doses of each GLE event on the surfaces of Mars (y-axes) and the Moon (x-axes). Both Martian and lunar results are shown in the logarithmic scale where we observe a good linear relation, with the Pearson correlation coefficient being 0.83. For studied GLE events, the Martian-surface brain dose y can be formulated as a function of the lunar-surface brain dose x using the linear least-squares fitting (the light blue line) as $\log(y) = 0.65 \cdot \log(x) - 3.20$. The standard error of two linear fit parameters are 0.28 and 0.06, respectively. A 90% confidence band of the fitting result is also shown in light blue range. Overall, there is a big difference, more than two orders of magnitude, between an event dose on Mars and that on the Moon. This is caused mainly by the Mars atmosphere which can effectively stop or slow down energetic protons with energy below a few hundreds of MeV.

The cerebrum, the largest and the main part of the brain, contains the cerebral cortex which is divided into four lobes: the frontal lobe, temporal lobe, parietal lobe, and occipital lobe. Each lobe is responsible for different functions, such as reading, movement, vision, etc. Therefore, it is necessary to obtain the dose in separate lobes to better evaluate astronauts' performance in certain functions. More details of the calculation procedure of dose in different lobes can be found in Khaksarighiri et al. (2020).

Figure 6b gives the correlation of GLE-induced lunar-surface dose and Martian-surface dose in the whole brain (blue dots), frontal lobe (red dots), parietal lobe (turquoise dots), temporal lobe (orange dots), and occipital lobe (green yellow dots). The frontal lobe is in the outer region of the brain and occupies the biggest portion of the brain, located just behind the forehead. The temporal lobe is located in the most medial part of the brain and is surrounded by other lobes. The dose in the lobes are less than those in the entire head by nearly one order of magnitude for both the Martian and lunar cases. This is due to the protection by the human cranium, which can serve as a good shielding against low-energy particles below ∼10 MeV (Khaksarighiri et al., 2020). For the outermost frontal lobe and the innermost temporal lobe, doses in them are generally close on Martian surface, while doses in the frontal lobe are higher than those in the temporal lobe on the lunar surface. In Figure 3, the most significant difference in the two planetary environments is the low-energy proton component (<200 MeV) in the downward direction. Located in the upper and frontal part of the head, the frontal lobe tends to withstand more radiation exposure from these low-energy protons which are more intense on the Moon. The dose correlation in the other two lobes (the parietal and occipital lobe) are similar to the frontal lobe and temporal lobe correlation, that their values are comparable on the Martian surface among different lobes, while the dose values in the parietal and occipital lobes on the lunar surface are in between those in the frontal (outermost) and temporal (innermost) lobes.

3.5. Varying Martian Atmospheric Shielding Effect and Extra Shielding Around the Head

During actual space missions, shielding will be adopted to protect the astronaut from radiation risk and the harsh space environment. For instance, the international space station provides at least 5 g/cm^2 of aluminum (Al)-equivalent shielding (Dastider et al., 2021). Personnel ionizing radiation protection is required by NASA Technical Standard (NASA, 2022), including launch, entry and abort suits and extravehicular activity suits that shall provide or accommodate radiation monitoring and alerting functions. To simulate a more mission-realistic situation, we calculate the average dose induced by radiation in the head shielded by the different thickness of Al, using BRFs under different shielding conditions (Khaksarighiri et al., 2020).

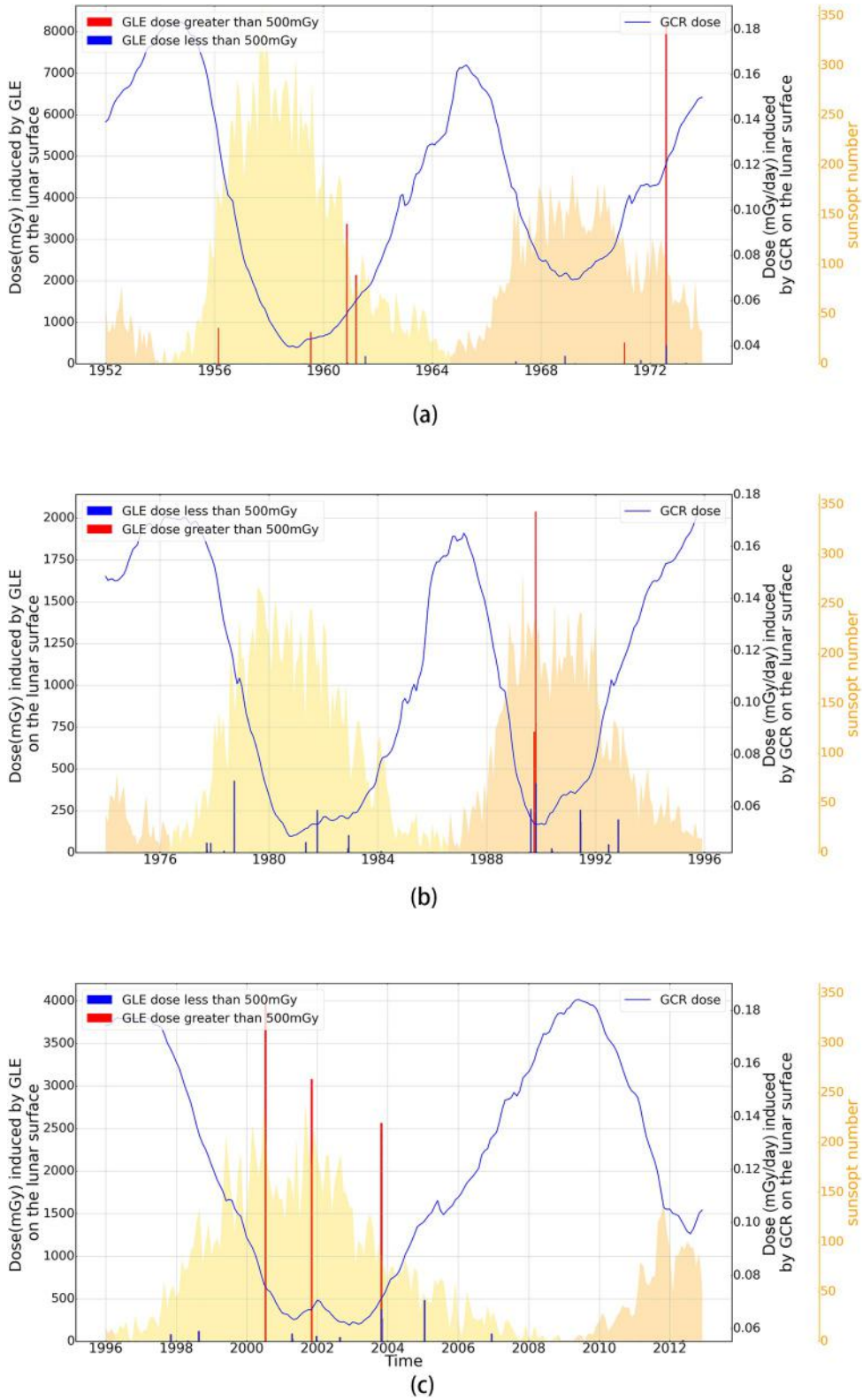

Figure 5. Long-term variations of dose (or dose rate) induced by Galactic Cosmic Rays (blue lines, right *y*-axes) and by each ground-level enhancement event (blue or red bars, left *y*-axes) over more than five solar cycles on the surface of the Moon. Sunspot numbers are plotted as yellow (odd cycle) and orange (even cycle) backgrounds.

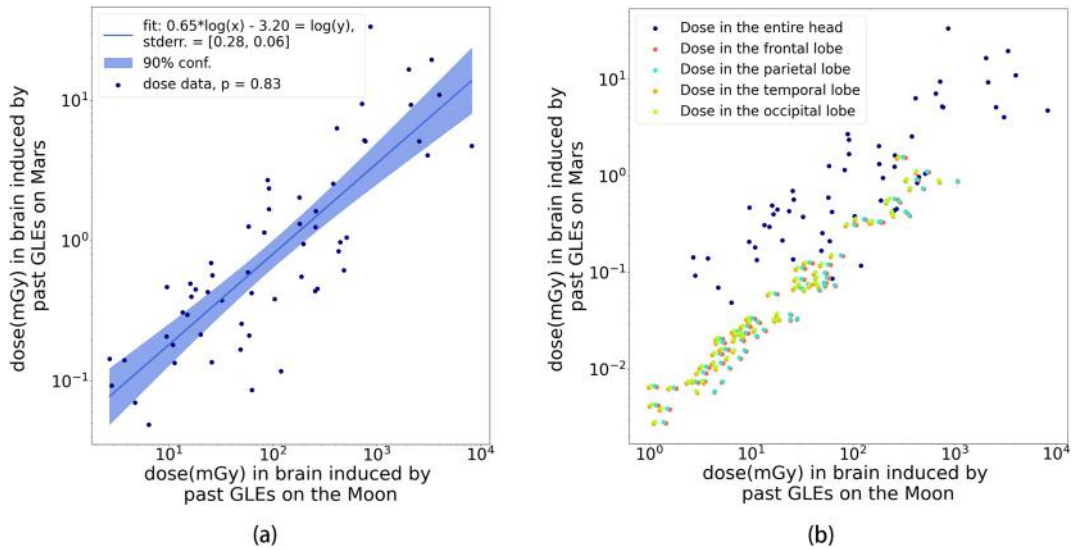

Figure 6. Correlation between the "brain doses" induced by past ground-level enhancement events on the Martian (*y*-axes) surface with a surface pressure of 827 Pa and on the lunar (*x*-axes) surface. (a): Each dot represents the result of an event; The blue line is the result of linear least-squares fit between the lunar and Martian results with the blue region denoting the 90% confidence band. The label "fit" in the legend gives the fitting parameter and function while "stderr" includes the standard errors of two fitting parameters. (b): Blue, red, turquoise, orange and green yellow dots denote the correlation of doses in the entire head and four lobes, respectively.

In addition to the Al shielding, the shielding effect of the Martian atmosphere has already been mentioned in Sections 3.1.1 and 3.1.2. The variation of the pressure due to the regional (mainly altitude-related) differences on Mars may range from below 100 Pa to more than 1,000 Pa. In a previous study based on the same Mars model, Zhang et al. (2022) showed that the quiet-time GCR radiation on the Martian surface is not very sensitive to the surface pressure. However, changes of the pressure may modulate the GLE flux that reach the Martian surface effectively, especially for surface pressures with a value lower than 400 Pa.

Figure 7 shows the three most extreme GLE events that induced the largest dose in deep space among past GLEs studied here. The gray error bars on the Martian surface doses show the dose variation range caused by the changes of the pressure from about 300 Pa (upper limit for the surface dose) and 1,200 Pa (lower limit for the surface dose). Martian surface doses are considerably below the risk threshold even when the surface pressure is

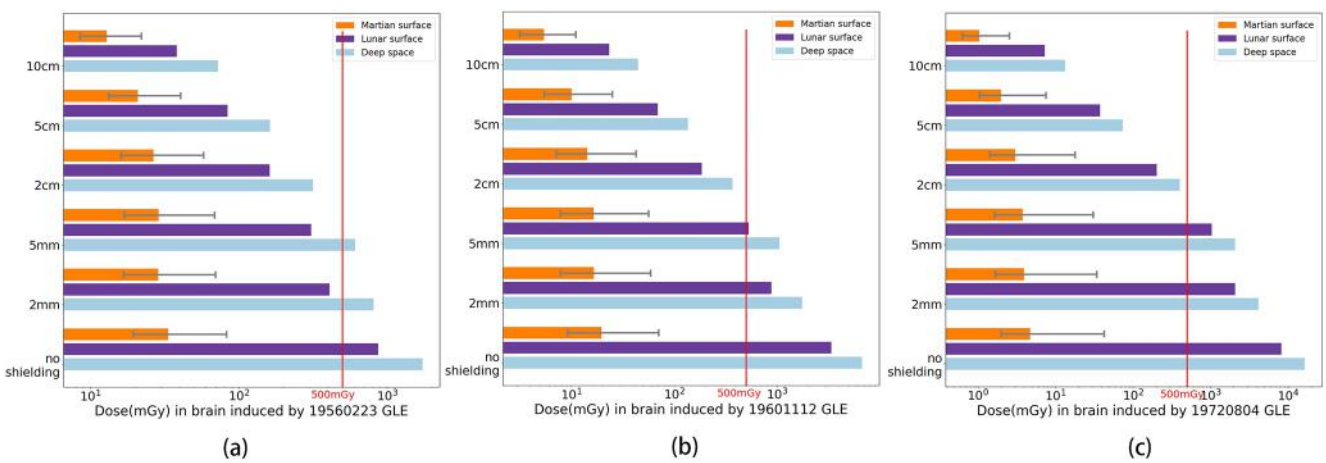

Figure 7. Event dose of three selected events (from left to right, ground-level enhancement event dates are 23 February 1956, 12 November 1960, and 4 August 1972) on the Martian surface with a surface pressure of 827 Pa (orange), on the lunar surface (purple) and in deep space (light blue) and the comparison of different results from different shielding scenarios. The vertical red line represents the 30-day dose upper limit in Central Nervous System defined by NASA which is 500 mGy. Error bars on the Martian dose results indicate the dose variation range due to the change of the Martian surface pressure from about 300 to 1,200 Pa.

low (300 Pa corresponds to a vertical column mass of about 8 g/cm^2), however, doses on the lunar surface and deep space can exceed the 500 mGy limit, if there is no adequate shielding protection. With a shielding thickness around 5 g/cm^2 (about 2 cm of Al) or above, all event-induced doses in the head would be reduced to a safe value for CNS both in deep space and on the lunar surface. However, these results are for single events, it is not unlikely that the accumulated dose of several events encountered during a long mission period may exceed the recommendation limit. We estimate the accumulated dose for 4 events during October 1989 on the lunar surface to be 361 mGy under 2 cm Al shielding or 983 mGy under 5 mm Al shielding. These values are comparable to the 500 mGy limit.

4. Summary and Discussion

The biological effects of space radiation involve most organs of the human body, in which the CNS and particularly the brain is paid with special attention due to possible neurocognitive impairment and motor dysfunction. A recent study by Khaksarighiri et al. (2020, 2021) utilized GEANT4 Monte-Carlo simulations and developed the BRFs, representing particle interaction with a realistic human head and brain structure. The BRFs provide the dose deposited by energetic particles with different types and energy in the head and in four cerebrum lobes of the brain. In this study, we adopt the AtRIS and the REDMoon models to obtain the radiation environment on the Martian and lunar surfaces, respectively, for both GCR and extreme SEP conditions. First, BON14 GCR model and most GLE events from 1956 to 2012, across five full solar cycles, are taken as the primary radiation sources in deep space. Next, these primary source spectra are convoluted with the AtRIS and the REDMoon matrices to obtain the surface radiation environment of the two planetary bodies. At last, doses in different cases (i.e., different brain regions or various shielding thicknesses) are obtained and compared with one another. Our main results are summarized below.

1. On the Martian surface with a pressure of 827 Pa without extra shielding, overall GCR-induced dose rate in a human head ranges from 0.032 to 0.120 mGy/day; the maximum GLE-induced dose value is 33 mGy/event (on 23 February 1956) and no GLE-induced event dose in this time range exceeds 500 mGy.
2. On the lunar surface without additional shielding, background GCR-induced doses rate ranges from 0.039 to 0.184 mGy/day; the maximum GLE-induced dose value is about 8,000 mGy/event (on 4 August 1972) and 13 out of 65 historical GLE-induced doses are greater than 500 mGy.
3. Doses induced by GLE events on the Martian surface with a pressure of 827 Pa have a good correlation with those on the lunar surface. A linear formula is fitted in the double-logarithmic scale for these two quantities. The dose values for different brain lobes are relatively similar on Mars, and the dose in the frontal lobe is slightly higher for GLE events on the Moon, due to its outermost position allowing for the access of low-energy particles which exist abundantly during SEP events.
4. When examining the dose levels of all 63 selected GLE events in the brain, we found that none of the events induced a dose reaching an alarmed limit on Mars. As for the cases of events on the lunar surface and in deep space, all of the GLE events studied here can be reduced to a safe level for CNS by >5 g/cm^2 of Al-equivalent shielding.

The current study hasn't considered the body part of a human being when evaluating the radiation impact on our brains. Based on a simple human phantom considering a Chinese male astronaut with an average height of 169 cm (whose geometry can be simplified as a spherical head with a radius of 11.5 cm on top of a cylinder (body) with a height of 145.5 cm and a radius of 18.8 cm below the sphere), we roughly estimate the solid angle blocked by the body is up to 0.22π. This is a rather small portion of the full solid angle (4π) surrounding the head. Thus the omission of the body part should not significantly influence the primary radiation arriving at the head. However, we still need to pay attention to the upward neutron flux generated in the body due to abundant water in our bodies. On the one hand, in an aqueous environment, oxygen radicals produced by radiation-induced disintegration can easily lead to more harmful chemical reactions (Allen et al., 1951; Martínez-Cayuela, 1995). On the other hand, water has been proven as a good modulator for fast neutrons, and water in our body may also lead to a reduction of the neutron contributed effective dose. Thus it is non-trivial to estimate if water in our body would increase or decrease the radiation impact on the head. Considering the above issues as well as the scattered rays of other secondaries from the body, a simulation with a full-body phantom is needed for a more accurate assessment of the radiation effects in the head.

Reitz et al. (2012) have simulated GCR proton, alpha, oxygen, Fe induced dose rate using an International Commission on Radiological Protection (ICRP) human-body phantom surrounded by 0.5 g/cm^2 polycarbonate shielding in the lunar surface environment. Their results of the brain dose under a solar minimum condition is

larger than ours by 0.05 mGy/day (around 30%) under the same shielding thickness (0.5 g/cm^2 of the Al). We consider this as a good agreement, given different model inputs and setups, such as different input GCR spectra, head geometry, shielding material, Lunar surface environment, GEANT4 physics list, and that we haven't accounted for the body geometry. They also showed that dose rate in other organs is not much of a difference from the brain dose rate and is all around 0.2 mGy/day.

Besides, during actual space missions, spacesuit geometries and the habitat structures will be surely more complicated than the aluminum-shell shielding employed in this work. Thus more realistic considerations of the mission scenario should be applied as well.

Finally, our results should be combined with biomedical research on mechanisms of radiation impact on the CNS to better understand the biological effect of space radiation on human brains. In addition, more focused studies and quantitative estimations of radiation in the hippocampus or spinal cord, would be helpful for better evaluating the radiation impact on critical brain functions such as learning and memory.

Data Availability Statement

The particle interactions with the Martian environment are calculated via the GEANT4-based AtRIS model which is uploaded at Zenodo platform (Banjac, 2019). The particle interactions with the Lunar environment are calculated via the REDMoon code which is also uploaded at Zenodo platform (Dobynde & Guo, 2021a). The Brain Response Functions used in this study have been developed by Khaksarighiri et al. (2020). Monthly averaged sunspot numbers (version 2.0) used in this study are obtained from Sunspot Index and Long-term Solar Observations (SILSO) dataset (SIDC, 2015).

Acknowledgments
We thank the anonymous reviewers for their helpful comments in helping us to improve the manuscript. We acknowledge the Strategic Priority Program of the Chinese Academy of Sciences (Grant XDB41000000), the National Natural Science Foundation of China (Grants 42188101, 42074222, 41941001) and the CNSA pre-research Project on Civil Aerospace Technologies (Grant D020104). SK and RFWS are supported in Germany by DLR (Grants 50QM0501, 50QM1201, and 50QM1701) to the CAU Kiel.

References

Acharya, M. M., Baulch, J. E., Klein, P. M., Baddour, A. A. D., Apodaca, L. A., Kramár, E. A., et al. (2019). New concerns for neurocognitive function during deep space exposures to chronic, low dose-rate, neutron radiation. *eNeuro*, *6*(4), 1–15. https://doi.org/10.1523/ENEURO.0094-19.2019

Adams, J., Bhattacharya, M., Lin, Z., Pendleton, G., & Watts, J. (2007). The ionizing radiation environment on the moon. *Advances in Space Research*, *40*(3), 338–341. https://doi.org/10.1016/j.asr.2007.05.032

Agostinelli, S., Allison, J., Amako, K., Apostolakis, J., Araujo, H., Arce, P., et al. (2003). GEANT4: A simulation toolkit. *Nuclear Instruments and Methods*, *A506*(3), 250–303. https://doi.org/10.1016/S0168-9002(03)01368-8

Allen, A. O., Hochanadel, C. J., Ghormley, J. A., & Davis, T. W. (1951). Decomposition of water and aqueous solutions under mixed fast neutron and gamma radiation. *The Journal of Physical Chemistry*, *56*(5), 575–586. https://doi.org/10.1021/j150497a007

Allison, J., Amako, K., Apostolakis, J., Araujo, H., Arce Dubois, P., Asai, M., et al. (2006). Geant4 developments and applications. *IEEE Transactions on Nuclear Science*, *53*(1), 270–278. https://doi.org/10.1109/TNS.2006.869826

Allison, J., Amako, K., Apostolakis, J., Arce, P., Asai, M., Aso, T., et al. (2016). Recent developments in Geant4. *Nuclear Instruments and Methods A*, *835*, 186–225. https://doi.org/10.1016/j.nima.2016.06.125

Banjac, S. (2019). Atmospheric radiation interaction simulator (AtRIS) [Software]. Zenodo. https://doi.org/10.5281/zenodo.3633451

Banjac, S., Herbst, K., & Heber, B. (2018). The atmospheric radiation interaction simulator (AtRIS)—Description and validation. *Journal of Geophysical Research: Space Physics*, *123*(ja), 50–67. https://doi.org/10.1029/2018JA026042

Battistoni, G., Boehlen, T., Cerutti, F., Chin, P. W., Esposito, L. S., Fassò, A., et al. (2015). Overview of the fluka code. *Annals of Nuclear Energy*, *82*, 10–18. (Joint International Conference on Supercomputing in Nuclear Applications and Monte Carlo 2013, SNA + MC 2013. Pluri- and Trans-disciplinarity, Towards New Modeling and Numerical Simulation Paradigms). https://doi.org/10.1016/j.anucene.2014.11.007

Boerma, M., Nelson, G. A., Sridharan, V., Mao, X.-W., Koturbash, I., & Hauer-Jensen, M. (2015). Space radiation and cardiovascular disease risk. *World Journal of Cardiology*, *7*(12), 882–888. https://doi.org/10.4330/wjc.v7.i12.882

Budinger, T. F., Lyman, J. T., & Tobias, C. A. (1972). Visual perception of accelerated nitrogen nuclei interacting with the human retina. *Nature*, *239*(5369), 209–211. https://doi.org/10.1038/239209a0

Chancellor, J. C., Scott, G. B., & Sutton, J. P. (2014). Space radiation: The number one risk to astronaut health beyond low Earth orbit. *Life*, *4*(3), 491–510. https://doi.org/10.3390/life4030491

Cliver, E. W., & Ling, A. G. (2001). 22 year patterns in the relationship of sunspot number and tilt angle to cosmic-ray intensity. *The Astrophysical Journal*, *551*(2), L189–L192. https://doi.org/10.1086/320022

Cucinotta, F. A. (2010). *Radiation risk acceptability and limitations*. Space Radiation Program Element, NASA Johnson Space Center. Retrieved from https://three.jsc.nasa.gov/articles/AstronautRadLimitsFC.pdf

Cucinotta, F. A., Alp, M., Sulzman, F. M., & Wang, M. (2014). Space radiation risks to the central nervous system. *Life Sciences and Space Research*, *2*, 54–69. https://doi.org/10.1016/j.lssr.2014.06.003

Curtis, S. B., Vazquez, M. E., Wilson, J. W., Atwell, W., Kim, M., & Capala, J. (1998). Cosmic ray hit frequencies in critical sites in the central nervous system. *Advances in Space Research*, *22*(2), 197–207. https://doi.org/10.1016/S0273-1177(98)80011-2

Dastider, A. G., Saha, S., Sukanya, M. I., & Chakraborty, R. (2021). Comparative analysis among materials for passive shielding in a manned mars mission. *Astrophysics and Space Science*, *366*(120), 120. https://doi.org/10.1007/s10509-021-04031-4

Delp, M. D., Charvat, J. M., Limoli, C. L., Globus, R. K., & Ghosh, P. (2016). Apollo lunar astronauts show higher cardiovascular disease mortality: Possible deep space radiation effects on the vascular endothelium. *Scientific Reports*, *6*(1), 29901. https://doi.org/10.1038/srep29901

Dobynde, M. I., & Guo, J. (2021a). Dataset for "radiation environment at the surface and subsurface of the Moon: Model development and validation" publication in Journal of Geophysical research: Planets [Dataset]. Zenodo. https://doi.org/10.5281/zenodo.5561427

Dobynde, M. I., & Guo, J. (2021b). Radiation environment at the surface and subsurface of the moon: Model development and validation. *Journal of Geophysical Research: Planets*, *126*(11), e2021JE006930. https://doi.org/10.1029/2021JE006930

Drake, B. G., Hoffman, S. J., & Beaty, D. W. (2010). Human exploration of mars, design reference architecture 5.0. In *2010 IEEE aerospace conference* (pp. 1–24). https://doi.org/10.1109/AERO.2010.5446736

Forget, F., Hourdin, F., Fournier, R., Hourdin, C., Talagrand, O., Collins, M., et al. (1999). Improved general circulation models of the Martian atmosphere from the surface to above 80 km. *Journal of Geophysical Research*, *104*(E10), 24155–24176. https://doi.org/10.1029/1999JE001025

Guo, J., Saša, B., Röstel, L., Terasa, J. C., Herbst, K., Heber, B., & Wimmer-Schweingruber, R. F. (2019). Implementation and validation of the GEANT4/AtRIS code to model the radiation environment at Mars. *Journal of Space Weather and Space Climate*, *9*, A2. https://doi.org/10.1051/swsc/2018051

Guo, J., Zeitlin, C., Wimmer-Schweingruber, R. F., Hassler, D. M., Ehresmann, B., Rafkin, S., et al. (2021). Radiation environment for future human exploration on the surface of Mars: The current understanding based on MSL/RAD dose measurements. *The Astronomy and Astrophysics Review*, *29*(1), 8. https://doi.org/10.1007/s00159-021-00136-5

Hassler, D. M., Zeitlin, C., Wimmer-Schweingruber, R. F., Ehresmann, B., Rafkin, S., Eigenbrode, J. L., et.al. (2014). Mars' surface radiation environment measured with the Mars Science Laboratory's Curiosity Rover. *Science*, *343*(6169), 1244797. https://doi.org/10.1126/science.1244797

Honig, T., Witasse, O. G., Evans, H., Nieminen, P., Kuulkers, E., Taylor, M. G., et al. (2019). Multi-point galactic cosmic ray measurements between 1 and 4.5 au over a full solar cycle. *Annales Geophysicae*, *37*(5), 903–918. https://doi.org/10.5194/angeo-37-903-2019

Hu, S., Kim, M.-H. Y., McClellan, G. E., & Cucinotta, F. A. (2009). Modeling the acute health effects of astronauts from exposure to large solar particle events. *Health Physics*, *96*(4), 465–476. https://doi.org/10.1097/01.HP.0000339020.92837.61

Huff Janice, J., Lisa, C., Steve, B., Lori, C., Kerry, G., Sarah, L., et al. (2016). Risk of radiation carcinogenesis: Human research program space radiation element. Retrieved from https://ntrs.nasa.gov/citations/20160004369

Jandial, R., Hoshide, R., Waters, J., & Limoli, C. L. (2018). Space–brain: The negative effects of space exposure on the central nervous system. *Surgical Neurology International*, *9*(9), 9. https://doi.org/10.4103/sni.sni_250_17

Khaksarighiri, S., Guo, J., Wimmer-Schweingruber, R., & Narici, L. (2021). An easy-to-use function to assess deep space radiation in human brains. *Scientific Reports*, *11*(1), 11687. https://doi.org/10.1038/s41598-021-90695-5

Khaksarighiri, S., Guo, J., Wimmer-Schweingruber, R., Narici, L., & Lohf, H. (2020). Calculation of dose distribution in a realistic brain structure and the indication of space radiation influence on human brains. *Life Sciences and Space Research*, *27*, 33–48. https://doi.org/10.1016/j.lssr.2020.07.003

Köhler, J., Zeitlin, C., Ehresmann, B., Wimmer-Schweingruber, R., Hassler, D., Reitz, G., et al. (2014). Measurements of the neutron spectrum on the Martian surface with MSL/RAD. *Journal of Geophysical Research: Planets*, *119*(3), 594–603. https://doi.org/10.1002/2013JE004539

Lonart, G., Parris, B., Johnson, A. M., Miles, S., Sanford, L. D., Singletary, S. J., & Britten, R. A. (2012). Executive function in rats is impaired by low (20 cGy) doses of 1 GeV/u ^{56}Fe particles. *Radiation Research*, *178*(4), 289–294. https://doi.org/10.1667/RR2862.1

Martínez-Cayuela, M. (1995). Oxygen free radicals and human disease. *Biochimie*, *77*(3), 147–161. https://doi.org/10.1016/0300-9084(96)88119-3

Matthiä, D., Ehresmann, B., Lohf, H., Köhler, J., Zeitlin, C., Appel, J., et al. (2016). The Martian surface radiation environment—A comparison of models and MSL/RAD measurements. *Journal of Space Weather and Space Climate*, *6*, A13. https://doi.org/10.1051/swsc/2016008

McKinney, G. W., Lawrence, D. J., Prettyman, T. H., Elphic, R. C., Feldman, W. C., & Hagerty, J. J. (2006). MCNPX benchmark for cosmic ray interactions with the moon. *Journal of Geophysical Research*, *111*(E6), E06004. https://doi.org/10.1029/2005JE002551

Miroshnichenko, L., Vashenyuk, E., & Pérez-Peraza, J. (2013). Solar cosmic rays: 70 years of ground-based observations. *Geomagnetism and Aeronomy*, *53*(5), 541–560. https://doi.org/10.1134/s0016793213050125

NASA. (2022). Space flight human-system standard volume 2, revision c: Human factors, habitability, and environmental health. Retrieved from https://standards.nasa.gov/sites/default/files/standards/NASA/C/2022-04-08-NASA-STD-3001-Vol-2-Rev-C-Final_0.pdf

O'Neill, P., Golge, S., & Slaba, T. (2015). *Badhwar–O'Neill 2014 galactic cosmic ray flux model* (p. 218569). NASA/TP. Retrieved from https://ntrs.nasa.gov/archive/nasa/casi.ntrs.nasa.gov/20150003026.pdf

Parihar, V. K., Allen, B. D., Caressi, C., Kwok, S., Chu, E., Tran, K. K., et al. (2016). Cosmic radiation exposure and persistent cognitive dysfunction. *Scientific Reports*, *6*(1), 34774. https://doi.org/10.1038/srep34774

Patel, Z. S., Brunstetter, T. J., Tarver, W. J., Whitmire, A. M., Zwart, S. R., Smith, S. M., & Huff, J. L. (2020). Red risks for a journey to the red planet: The highest priority human health risks for a mission to Mars. *npj Microgravity*, *6*(1), 33. https://doi.org/10.1038/s41526-020-00124-6

Potgieter, M. S. (2013). Solar modulation of cosmic rays. *Living Reviews in Solar Physics*, *10*(1), 1–66. https://doi.org/10.12942/lrsp-2013-3

Raukunen, O., Vainio, R., Tylka, A. J., Dietrich, W. F., Jiggens, P., Heynderickx, D., et al. (2018). Two solar proton fluence models based on ground level enhancement observations. *Journal of Space Weather and Space Climate*, *8*, A04. https://doi.org/10.1051/swsc/2017031

Reitz, G., Berger, T., & Matthiae, D. (2012). Radiation exposure in the moon environment. *Planetary and Space Science*, *74*(1), 78–83. (Scientific Preparations For Lunar Exploration). https://doi.org/10.1016/j.pss.2012.07.014

Rivera, P. D., Shih, H.-Y., LeBlanc, J. A., Cole, M. G., Amaral, W. Z., Mukherjee, S., et al. (2013). Acute and fractionated exposure to high-LET ^{56}Fe HZE-particle radiation both result in similar long-term deficits in adult hippocampal neurogenesis. *Radiation Research*, *180*(6), 658–667. https://doi.org/10.1667/RR13480.1

Röstel, L., Guo, J., Banjac, S., Wimmer-Schweingruber, R. F., & Heber, B. (2020). Subsurface radiation environment of mars and its implication for shielding protection of future habitats. *Journal of Geophysical Research: Planets*, *125*(3), e2019JE006246. https://doi.org/10.1029/2019JE006246

Roussos, E., Dialynas, K., Krupp, N., Kollmann, P., Paranicas, C., Roelof, E. C., et al. (2020). Long- and short-term variability of galactic cosmic-ray radial intensity gradients between 1 and 9.5 au: Observations by Cassini, BESS, BESS-Polar, PAMELA, and AMS-02. *The Astrophysical Journal*, *904*(2), 165. https://doi.org/10.3847/1538-4357/abc346

Sato, T., Niita, K., Matsuda, N., Hashimoto, S., Iwamoto, Y., Noda, S., et al. (2013). Particle and heavy ion transport code system, PHITS, version 2.52. *Journal of Nuclear Science and Technology*, *50*(9), 913–923. https://doi.org/10.1080/00223131.2013.814553

SIDC. (2015). Monthly mean total sunspot number from sunspot index and long-term solar observations, Royal observatory of Belgium [Dataset]. WDC-SILSO. Retrieved from https://sidc.be/silso/DATA/SN_m_tot_V2.0.txt

Simpson, J. (1983). Elemental and isotopic composition of the galactic cosmic rays. *Annual Review of Nuclear and Particle Science*, *33*(1), 323–382. https://doi.org/10.1146/annurev.ns.33.120183.001543

Slaba, T. C., Wilson, J. W., Badavi, F. F., Reddell, B. D., & Bahadori, A. A. (2016). Solar proton exposure of an ICRU sphere within a complex structure part II: Ray-trace geometry. *Life Sciences and Space Research*, *9*, 77–83. https://doi.org/10.1016/j.lssr.2016.05.001

Smith, M., Craig, D., Herrmann, N., Mahoney, E., Krezel, J., McIntyre, N., & Goodliff, K. (2020). The Artemis program: An overview of NASA's activities to return humans to the moon. In *2020 IEEE aerospace conference* (pp. 1–10). https://doi.org/10.1109/AERO47225.2020.9172323

Thomas, S. R., Owens, M. J., & Lockwood, M. (2014). The 22-year hale cycle in cosmic ray flux–evidence for direct heliospheric modulation. *Solar Physics*, *289*(1), 407–421. https://doi.org/10.1007/s11207-013-0341-5

Wang, Y., Guo, J., Li, G., Roussos, E., & Zhao, J. (2022). Variation in cosmic-ray intensity lags sunspot number: Implications of late opening of solar magnetic field. *The Astrophysical Journal*, *928*(2), 157. https://doi.org/10.3847/1538-4357/ac5896

Werner, C. J., Armstrong, J. C., Brown, F. B., Bull, J. S., Casswell, L., Cox, L., et al. (2017). MCNP users manual-code version 6.2. Retrieved from https://mcnp.lanl.gov/mcnp_manual.shtml

Wilson, J. W., Slaba, T. C., Badavi, F. F., Reddell, B. D., & Bahadori, A. A. (2016). Solar proton exposure of an ICRU sphere within a complex structure: Combinatorial geometry. *Life Sciences and Space Research*, *9*, 69–76. https://doi.org/10.1016/j.lssr.2016.05.002

Wu, H., Huff, J., Casey, R., Kim, M., & Cucinotta, F. (2013). *Evidence report: Risk of acute radiation syndromes due to solar particle events*. National Aeronautical and Space Agency. Retrieved from https://humanresearchroadmap.nasa.gov/Evidence/reports/ars.pdf

Zaman, F. A., Townsend, L. W., de Wet, W. C., Looper, M. D., Brittingham, J. M., Burahmah, N. T., et al. (2022). Modeling the lunar radiation environment: A comparison among FLUKA, Geant4, HETC-HEDS, MCNP6, and PHITS. *Space Weather*, *20*(8), e2021SW002895. https://doi.org/10.1029/2021SW002895

Zhang, J., Guo, J., Dobynde, M. I., Wang, Y., & Wimmer-Schweingruber, R. F. (2022). From the top of Martian Olympus to deep craters and beneath: Mars radiation environment under different atmospheric and regolith depths. *Journal of Geophysical Research: Planets*, *127*(3), e2021JE007157. https://doi.org/10.1029/2021JE007157